EARTH SURFACE PROCESSES AND LANDFORMS
*Earth Surf. Process. Landforms* **39**, 366–380 (2014)

Published online 13 January 2014 in Wiley Online Library
(wileyonlinelibrary.com) DOI: 10.1002/esp.3502

# Geophysical constraints on deep weathering and water storage potential in the Southern Sierra Critical Zone Observatory

**W. Steven Holbrook,[1]* Clifford S. Riebe,[1] Mehrez Elwaseif,[1] Jorden L. Hayes,[1] Kyle Basler-Reeder,[2] Dennis L. Harry,[2] Armen Malazian,[3] Anthony Dosseto,[4] Peter C. Hartsough[3] and Jan W. Hopmans[3]**
[1] Department of Geology and Geophysics, University of Wyoming, Laramie, WY, USA
[2] Department of Geosciences, Warner College of Natural Resources, Colorado State University, Fort Collins, CO, USA
[3] Department of Land, Air and Water Resources, University of California, Davis, CA, USA
[4] Wollongong Isotope Geochronology Laboratory, School of Earth and Environmental Sciences, University of Wollongong, Wollongong, Australia

Received 20 March 2012; Revised 14 October 2013; Accepted 31 October 2013

*Correspondence to: W. Steven Holbrook, Department of Geology and Geophysics, University of Wyoming, Laramie, WY 82071, USA. E-mail: steveh@uwyo.edu

ESPL
Earth Surface Processes and Landforms

ABSTRACT: The conversion of bedrock to regolith marks the inception of critical zone processes, but the factors that regulate it remain poorly understood. Although the thickness and degree of weathering of regolith are widely thought to be important regulators of the development of regolith and its water-storage potential, the functional relationships between regolith properties and the processes that generate it remain poorly documented. This is due in part to the fact that regolith is difficult to characterize by direct observations over the broad scales needed for process-based understanding of the critical zone. Here we use seismic refraction and resistivity imaging techniques to estimate variations in regolith thickness and porosity across a forested slope and swampy meadow in the Southern Sierra Critical Zone Observatory (SSCZO). Inferred seismic velocities and electrical resistivities image a weathering zone ranging in thickness from 10 to 35 m (average = 23 m) along one intensively studied transect. The inferred weathering zone consists of roughly equal thicknesses of saprolite (P-velocity $< 2$ km s$^{-1}$) and moderately weathered bedrock (P-velocity = 2–4 km s$^{-1}$). A minimum-porosity model assuming dry pore space shows porosities as high as 50% near the surface, decreasing to near zero at the base of weathered rock. Physical properties of saprolite samples from hand augering and push cores are consistent with our rock physics model when variations in pore saturation are taken into account. Our results indicate that saprolite is a crucial reservoir of water, potentially storing an average of 3 m$^3$ m$^{-2}$ of water along a forested slope in the headwaters of the SSCZO. When coupled with published erosion rates from cosmogenic nuclides, our geophysical estimates of weathering zone thickness imply regolith residence times on the order of $10^5$ years. Thus, soils at the surface today may integrate weathering over glacial–interglacial fluctuations in climate. Copyright © 2013 John Wiley & Sons, Ltd.

KEYWORDS: geophysics; water storage; critical zone

## Introduction

In hilly and mountainous landscapes, bedrock breaks down in a complex interplay of physical, chemical, and biological processes. Damage from fracturing (e.g. Molnar *et al.*, 2007; Clarke and Burbank, 2011), frost cracking (Anderson *et al.*, 2013) and other mechanical processes enables subsurface penetration and throughflow of meteoric water. This in turn promotes chemical leaching, which causes solute losses (e.g. Stonestrom *et al.*, 1998; Buss *et al.*, 2008) and enhances the residuum's susceptibility to further weathering and erosion (Dixon *et al.*, 2009). Add life, and the transformation from rock to soil is complete; tree roots pry remaining rock apart and, together with symbiotic fungi, exude organic compounds that liberate life-sustaining nutrients from minerals and generate water-holding pore space in the mycorrhizosphere (Banfield *et al.*, 1999; Hubbert *et al.*, 2001; Landeweert *et al.*, 2001; Graham *et al.*, 2010).

Regolith, which here refers collectively to saprolite and soil, is the foundation for life in the 'critical zone' (CZ) (see Figure 1 for definitions). Its creation by subsurface weathering is counteracted by losses due to chemical erosion at depth and by both chemical and physical erosion near the surface (Dixon *et al.*, 2009; Riebe and Granger, 2013). The resulting competition between the creation and removal of regolith ultimately sets its thickness and degree of weathering (e.g. Stallard, 1985; Anderson *et al.*, 2007; Lebedeva *et al.*, 2010). For example, if erosion is fast and weathering is slow, such that the system is 'weathering-limited' (Carson and Kirkby, 1972; Stallard and Edmond, 1983), regolith is typically thin and not extensively weathered. Alternatively, if erosion is slow and weathering is fast, such that the system is 'transport-limited', regolith is typically thick and may be extensively weathered, due to long residence times afforded by slow removal rates. In this context, regolith is a residuum that can be interpreted in terms of

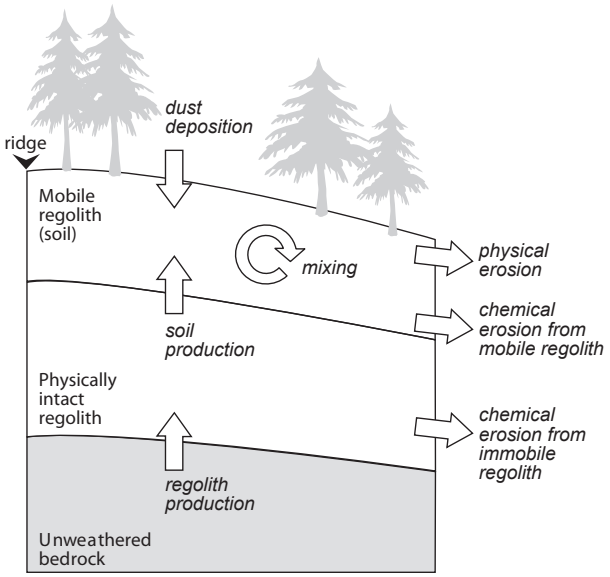


**Figure 1.** Concept sketch showing material components and fluxes of the 'critical zone' (CZ), which here refers inclusively to regolith and overlying vegetation, following widespread use of the term in the literature (National Research Council, 2001; Brantley *et al.*, 2011). Regolith is the heterogeneous interface between air and rock – a blanket of weathered material that includes saprolite and soil. Its thickness changes when there is an imbalance between inputs and outputs (denoted by arrows). Soil refers to the uppermost, mobile layer of weathered rock, organic detritus, and allochthonous dust, without regard to its degree of chemical alteration and horizonation. It is generated from above, by dust deposition, and from below, by breakdown of physically intact regolith. Transport downslope results in mixing; losses occur by chemical and physical erosion. Intact regolith, which may include both saprolite and weathered bedrock, differs from overlying soil in that it is physically intact enough to retain the fabric of underlying unweathered bedrock. The production of regolith at the rock–regolith interface is counteracted by losses due to production of soil and chemical erosion.

the processes that created it (Stallard and Edmond, 1983). Yet regolith is not just a residuum, but also a matrix of CZ processes. Hence regolith influences as well as reflects the balance between weathering and erosion. For example, rates of soil production have often been observed to decrease with increasing soil thickness (Heimsath *et al.*, 2012), consistent with the hypothesis that saprolite blanketed by thinner soils should be exposed to more frequent, intenser disruption by the biophysical processes that produce soil (Gilbert, 1877). This carries with it a negative feedback that may stabilize soils against wide fluctuations in thickness (Dietrich *et al.*, 1995); changes in soil thickness are self-arresting due to their offsetting influence on soil production rates. Similar feedbacks between surface and subsurface processes may help regulate the thickness of the regolith as a whole (Lebedeva *et al.*, 2010). For example, regolith production in the Rio Blanco Quartz Diorite (in Puerto Rico) appears to be driven by biotite oxidation in the presence of dissolved oxygen, which varies in porewaters as a function of depth in saprolite (Buss *et al.*, 2008). This suggests that regolith thickness may regulate regolith production rates in a hydro-geochemical feedback. Mechanisms such as this may help explain the growing body of empirical evidence from sites spanning a range of conditions that regolith properties may often play a role in setting the pace of regolith production (Dosseto *et al.*, 2008; Ma *et al.*, 2010; Dosseto *et al.*, 2012). Understanding precisely how is fundamental to process-based understanding of CZ formation and evolution. Making progress on this challenging problem requires knowledge of how the thickness and degree of alteration of regolith vary across landscapes (Braun *et al.*, 2009; Brantley *et al.*, 2011).

Probing regolith over scales appropriate to process-based studies of the CZ is challenging. Regolith is often tens of meters thick and highly variable in space. Drilling can be expensive and provides point samples that may not be representative of the surrounding regolith. Digging pits and augering by hand is less expensive and easier to apply over broad scales (e.g. Heimsath *et al.*, 1997; Burke *et al.*, 2007) but these methods typically fail to access the deepest reaches of weathering, which may often extend many tens of meters beneath the surface (e.g. Ruxton and Berry, 1957; Anderson *et al.*, 2002; Buss *et al.*, 2013). In contrast, application of geophysical techniques can inexpensively probe the deep subsurface and thus quantify physical properties that reflect weathering and water storage over broad areas. For example, P-wave velocities, which can be readily measured in slope-spanning seismic refraction surveys, are influenced by mineralogy, porosity, and density. Variations in these factors reflect variations in weathering with depth (e.g. Befus *et al.*, 2011) and may also mark major subsurface boundaries, including the bedrock–regolith interface. Electrical resistivity, which can also be measured in slope-spanning surveys, is influenced by subsurface concentrations of water, dissolved salts (e.g. Saarenketo, 1998), and clay (e.g. Samouëlian *et al.*, 2005), which reflect mass loss (and thus the opening of pores) and the degree of alteration due to subsurface weathering (Braun *et al.*, 2009). Thus, when used separately or together, resistivity and seismic refraction surveys can put quantitative constraints on weathering and water-storage potential in landscapes (e.g. Beylich *et al.*, 2003, 2004; Gallardo and Meju, 2003, 2004; Heincke *et al.*, 2010; Olona *et al.*, 2010; McClymont *et al.*, 2011).

Here we present results of geophysical investigations of subsurface weathering and water-storage potential in the Southern Sierra Critical Zone Observatory (SSCZO), which is one of a growing network of multi-institutional, cross-disciplinary sites for long-term research on CZ processes (Anderson *et al.*, 2008). While geophysical studies of the near surface are increasingly common (e.g. Robinson *et al.*, 2008; Knight *et al.*, 2010), our work is the first of its kind at the SSCZO. Thus it provides a crucial dataset for understanding the role of subsurface weathering in ecosystem dynamics, landscape evolution, and the water cycle. Our work is unique in applying a rock physics model, based on Hertz–Mindlin contact theory, to quantitatively predict subsurface porosity distribution from seismic refraction velocities. We find that seismic velocity and electrical resistivity data are consistent with a weathering zone that has an average thickness of 23 m along a transect spanning a heavily instrumented, forested slope and swampy meadow in the headwaters of one of the main SSCZO study catchments. Porosities from the rock physics model are as high as 50%, decreasing with depth (where velocities are higher) and assumed clay content in the model. Model-predicted porosities are broadly consistent with those measured from physical properties of saprolite. This suggests that our analysis of the geophysical data provides robust first-order constraints on subsurface weathering and water storage potential along the transect. Our results indicate that saprolite is a crucial reservoir of water, with capacity for up to 5 $m^3/m^2$ of water storage in the subsurface of a forested slope in the SSCZO. We couple our geophysical estimates of regolith thickness with erosion rates from previously published cosmogenic nuclide studies to put first-order constraints on the timescales of weathering in the landscape. We find that the soils at the surface reflect weathering and erosion averaged over hundreds of thousands of years, implying that they integrate over the wide fluctuations in climate associated with multiple interglacial–glacial intervals.

## Setting

The SSCZO is located in Fresno County, California, USA, in granitic bedrock. It lies outside the limits of recent glaciation, in the heart of the so called 'stepped topography' (Wahrhaftig, 1965; Jessup *et al.*, 2011), a sequence of range-parallel ridges and valleys, with alternating steep and gentle terrain. Roadcuts in the area typically expose a sequence of saprolite overlying fresh granite. This suggests that variations in geophysical properties of the subsurface may often be straightforwardly interpreted to reflect variations in porosity and secondary mineral abundance.

The SSCZO lies within the Kings River Experimental Watershed (KREW), a site of long-term research by the Pacific Southwest Research Station of the US Forest Service (Hunsaker and Eagan, 2003). We focused on P301, one of three ~1 $km^2$ area SSCZO catchments at the head of Providence Creek (Figure 2A), which is part of the Kings River drainage. Vegetative cover, where present, is dominated by a mixed-conifer forest consisting of white fir (*Abies concolor*), ponderosa pine (*Pinus ponderosa*), Jeffrey pine (*Pinus jeffreyi*), black oak (*Quercus kelloggii*), sugar pine (*Pinus lambertiana*) and incense cedar (*Calocedrus decurrens*), with minor cover by mixed chaparral. Soils in P301 have highly variable thickness (that is, depth to saprolite) but are generally 1 m thick (Johnson *et al.*, 2011). Cosmogenic nuclides in the top of saprolite on a nearby slope yield soil production rates that range from 73 to 136 t $km^{-2}$ $yr^{-1}$ (Dixon *et al.*, 2009). Chemical erosion appears to account for ~40% or more (Dixon *et al.*, 2009) of overall denudation (that is, physical plus chemical erosion) at the site, and roughly half of all chemical erosion occurs in saprolite (Riebe and Granger, 2013). Mean annual precipitation is approximately 1100 mm $yr^{-1}$ (Hunsaker *et al.*, 2012) and mean annual temperature is approximately 9 °C. The style of precipitation varies from dominantly snow-derived in catchment headwaters to dominantly rain-derived at the catchment mouths (Bales *et al.*, 2011).

An improved understanding of the water balance at catchment scales is a major research goal of the SSCZO (Anderson *et al.*, 2008; Bales *et al.*, 2011). Of particular interest are data and analyses that help partition water fluxes into deep and shallow components. Another goal is to explore implications of subsurface water flow and storage for the ecosystem, including questions about the sources of water for vegetation and how they change throughout the year (Lin *et al.*, 2011). Observations of soil moisture, snow pack, and sap flow from a heavily instrumented white fir tree (CZT-1) show that roughly one third of its annual evapotranspiration is derived from depths > 1 m (Bales *et al.*, 2011), suggesting that water storage and throughflow in the deep subsurface may be a major component of the overall water budget for the ecosystem. We used our geophysical measurements, described next, to characterize the water storage capacity in the SSCZO at the hillslope scale.

## Acquisition and Processing of Data and Samples

### Geophysical survey design

Here we present data from two lines. Line 5 is a transect spanning a ridgetop, a forested hillslope and an open meadow (Figure 2), on which we acquired both seismic refraction and electrical resistivity data. The transect crosses within 5 m of CZT-1 (Bales *et al.*, 2011). The survey is underlain by the Dinkey Creek pluton (Bateman and Wones, 1972), a fairly uniform, medium-grained hornblende-biotite granodiorite, with abundant fist-sized (and smaller), disc-shaped mafic inclusions. The second line (Line 9) was situated on a bare expanse of the Bald Mountain pluton (Bateman and Wones, 1972), which is also medium grained, but devoid of hornblende and mafic inclusions. This line was sampled to constrain velocities of what we refer to as 'unweathered' bedrock; though the surface exhibits minor alteration of biotite and feldspar and modest fracturing and sheet jointing, it rings to the hammer and overall, appears to be as fresh as rock gets at the surface in the area. Topography was surveyed on each line using a tape measure and inclinometer; we estimate the accuracy in the surveyed positions to be ±0.2 m (horizontally and vertically), which is sufficiently accurate for the geophysical methods used here.

### Seismic refraction surveys and tomographic inversions

We acquired seismic refraction data on Line 5 using two 24-channel Geometrics Geode systems and 40 Hz vertical-component geophones spaced at 5 m, with a 12-pound sledgehammer source striking a ~20 cm × 20 cm × 2 cm-thick stainless steel plate. In some instances we supplemented data acquisition with 12-gauge shotgun blanks fired from a stainless-steel muzzle implanted 1–2 m deep in 5 cm-diameter auger holes. On Line 9, 24 geophones at 3 m spacing were attached to the outcrop using plaster of paris, and sledgehammer blows were landed directly on the outcrop. Shot spacing was ~15 m on Line 5 and 6 m on Line 9.

We produced seismic velocity models using first-arrival, travel-time tomography. First arrival times were picked manually on all traces with sufficient signal-to-noise ratios. An example from each line is shown in Figure 3. Travel times were inverted

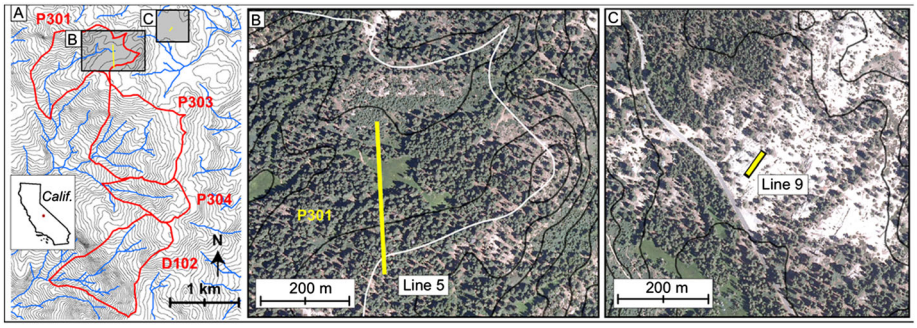


**Figure 2.** Location map, showing SSCZO catchments (A), which drain to Providence and Duff creeks in granitic terrain of the southern Sierra Nevada. Line 5 is located at the head of catchment P301 (with drainage divide shown in white), spanning a heavily instrumented swampy meadow and forested slope (B). Line 9 (C) spans an expanse of bare bedrock near Glen Meadow. Contour interval (black lines) is 10 m in each panel. This figure is available in colour online at wileyonlinelibrary.com/journal/espl

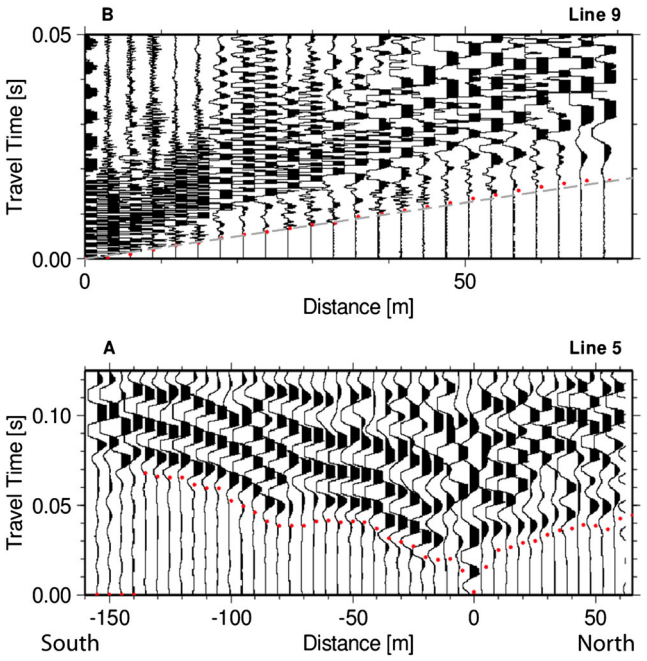


**Figure 3.** Seismic refraction data from geophones for one set of stacked records from (A) Line 5, and (B) Line 9. *X* Axis is distance away from source at $X=0$. Data quality is typical of stacked shots at other locations and is generally sufficient for straightforward manual picking of first arrivals (here marked by dots on each plot). Dashed line on data from Line 9, which spans a bare bedrock ridge, has a slope of 4 km s$^{-1}$ and is consistent with manually picked first arrivals. The same strong match to a 4 km s$^{-1}$ slope can be seen on all of the stacked records for Line 9, implying that 4 km s$^{-1}$ at depth is representative of minimally altered and fractured granite at the site. Note scale change between the data plots. This figure is available in colour online at wileyonlinelibrary.com/journal/espl

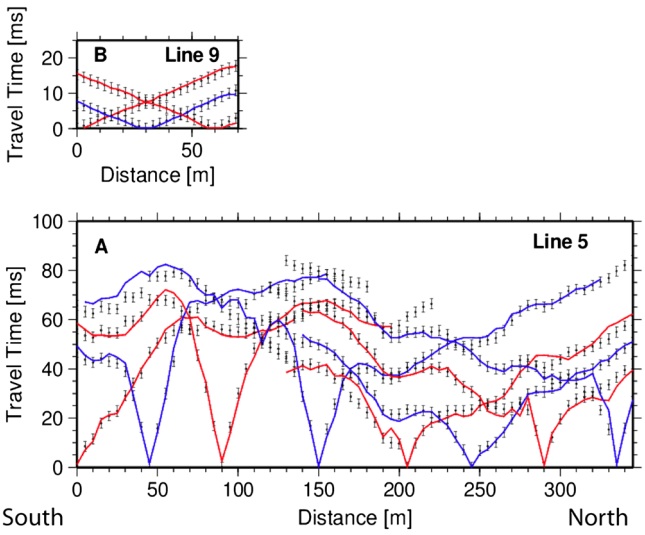


**Figure 4.** Travel time plots for (A) Line 5 and (B) Line 9, showing observed first-arrival travel times (dots with error bars) and predicted travel times based on the best-fit velocity models (red or blue lines). The observed and predicted travel times match well, suggesting that the inverted velocity model (Figure 5) is acceptable. To maintain clarity, only a subset (about 20%) of the shots are plotted here. Note scale change between plots. This figure is available in colour online at wileyonlinelibrary.com/journal/espl

for each line using SeisImager© software as follows. First, an initial velocity model was generated by inserting a uniform vertical velocity gradient (usually from 300 to 4500 m s$^{-1}$) beneath the elevation profile on the line. For the tomographic inversion, the model is discretized into cells of constant velocity; cell dimensions were constant in the horizontal (3 m for Line 9 and 5 m for Line 5) and varied in the vertical from about 2 to 6 m. Rays were traced by the shortest path method (Moser, 1991) from each shot to each receiver. The inversion was performed using an L2-norm non-linear least square algorithm, where the objective is to minimize the squares of the differences between the measured and modeled first-arrival travel-time data. The inversion typically results in smooth boundaries between regions with different velocity values. The convergence criteria are based on reaching the maximum allowed number of iterations or a user defined tolerance for the minimum change in root-mean-square (RMS) error from one iteration to the next. Ten iterations of a linearized least-squares inversion algorithm were conducted. No horizontal or vertical smoothing to the velocity cells was applied during the inversion. Typical agreement between predicted and observed travel times is shown in Figure 4. Agreement is generally lower for longer travel times, which reflect information from the deepest parts of the profile; here, ray coverage is lowest and thus provides least constraints on the inversion. The deepest penetration by ray paths on Line 5 is ~40 m, dictated mostly by the overall length of the geophone array in the survey.

Line 9 (Figure 2C) was acquired to identify the velocity that corresponds to relatively unweathered rock exposed on an extensive outcrop. The data on Line 9 differ from those on Line 5 in two important ways. First, at small source-receiver offsets, the first arrivals have nearly linear slopes that indicate velocities of ~4.0 km s$^{-1}$ at the surface (dashed line, Figure 3B). Second, the first arrivals have a high frequency content, with a center frequency around 400 Hz. In contrast, data from Line 5 have much slower first-arrival velocities and a lower frequency content, with a typical center frequency around 50 Hz. These characteristics are consistent with a unweathered bedrock with a nearly uniform velocity of 4.0 km s$^{-1}$ and low attenuation in the subsurface. This observation, together with several lines of evidence presented later, enables us to interpret velocities of 4.0 km s$^{-1}$ in the subsurface of other lines as 'pristine' bedrock.

In a linearized inversion, the final result can be highly dependent on the starting model. The starting model must be realistic (that is, capture the velocity range of subsurface materials at the survey site) in order for the inversion to converge to a realistic solution. Moreover, the final result will often carry vestiges of the starting model. For example, a starting model that consists of a simple linear increase in velocity with depth will generally produce a smoother final model than a layered starting model, which will often lead to a final model that retains sharp velocity increases where the original velocity steps were. We use a simple linear gradient in velocity for our starting models in the absence of *a priori* knowledge of any sharp transitions in velocity with depth.

Our tomographic inversion of seismic refraction data from Line 5 yields the velocity model shown in Figure 5A. To quantify the sensitivity of the inversion to the initial velocity model, we conducted a sensitivity analysis on Line 5. This involved 50 independent inversions from a suite of starting velocity models, chosen based on the expected velocity range of subsurface materials, wherein velocity increases linearly with depth from 0 to 50 m (Figure 6). Velocities at the surface and at 50 m depth were varied from 300 to 700 m s$^{-1}$, and from 3000 to 5300 m s$^{-1}$, respectively, resulting in a total velocity variation among starting models of about 800 m s$^{-1}$ at 10 m depth, 1000 m s$^{-1}$ at 20 m depth, and 1500 m s$^{-1}$ at 30 m depth (Figure 6). Velocity inversion parameters were held constant for all runs. The distribution of variance in modeled velocities is shown both in terms of percent error and in standard deviation in Figure 6. Percent errors are typically ~5–10%, with velocity uncertainties of ±100 m s$^{-1}$ in the upper 10 m and ±300 m s$^{-1}$ or more elsewhere. The sensitivity analysis suggests that our tomographic inversion of Line 5 is not highly sensitive to variations in the vertical gradient of the starting model.

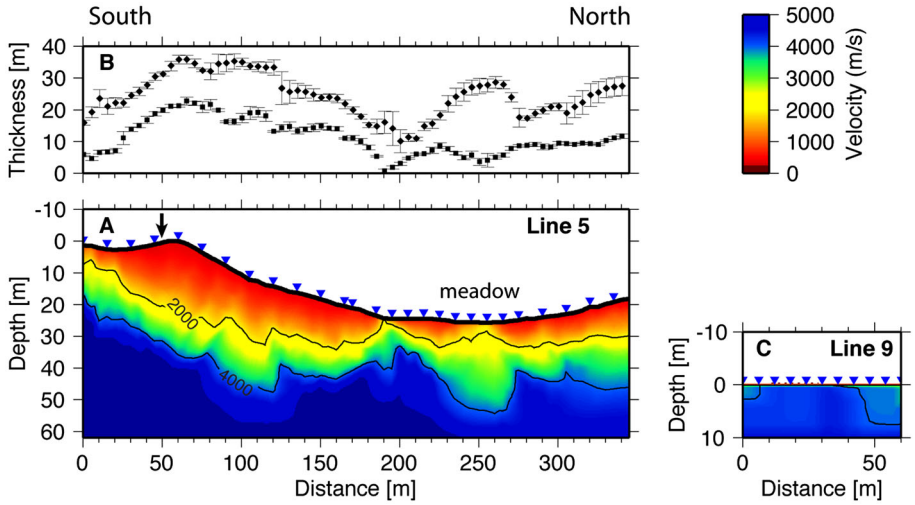


**Figure 5.** (A) Velocity model of Line 5 (Figure 2B) from inversion of first-arrival travel times. (B) Depth from the surface to the 2000 and 4000 m $s^{-1}$ contours. Error bars reflect variations observed in an ensemble of solutions that result from a range of starting models (see text). Depth to the 4000 m $s^{-1}$ contour varies from 10 to 35 m (average 23 m) and is highest at the crest of the forested slope, under CZT-1 (denoted by arrow), a heavily instrumented white fir. In contrast, under the swampy meadow, depth to the 4000 m $s^{-1}$ contour is shallowest and most variable, ranging from ~10 to 30 m over just 60 m of horizontal distance. (C) Velocity model of Line 9 from inversion of first-arrival travel times. Velocities of 4000 m $s^{-1}$ at the surface on Line 9, acquired on an extensive granite outcrop (Figure 2C), enable interpretation of 4000 m $s^{-1}$ velocities (blue shades) on Line 5 as coherent bedrock at depth. This figure is available in colour online at wileyonlinelibrary.com/journal/espl

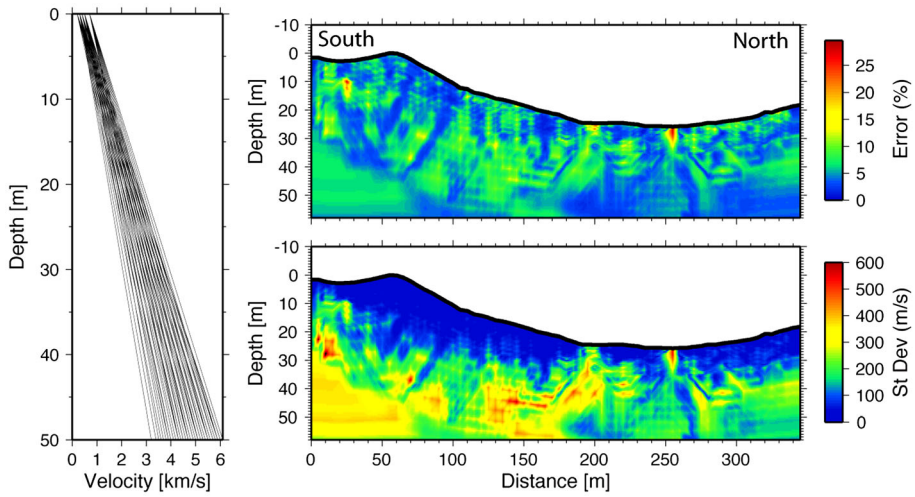


**Figure 6.** Results of sensitivity analysis of uncertainties in seismic velocity on Line 5. (Left) Velocity–depth gradients (in depth below surface) of 50 starting models used to generate ensemble of inverted models. (Right) Variance among final inversion in ensemble, expressed as standard deviation (bottom) and percent error (top). Velocity sensitivity in the upper 10 m is generally ±100 m $s^{-1}$ or less, and ±300 m $s^{-1}$ or more elsewhere. This figure is available in colour online at wileyonlinelibrary.com/journal/espl

## Electrical resistivity measurements and modeling

Electricial resistivity tomography is commonly applied to image subsurface structures with a detectable electrical resistivity contrast relative to the host medium. Because they are sensitive to electrical conductivity (or, equivalently, resistivity) rather than elastic properties (for example, velocity), electrical data can complement seismic refraction data in the interpretation of CZ architecture. In particular, resistivity values can help distinguish between two possible causes for increased seismic velocity: decreasing porosity (that is, less weathering) or increasing saturation of the pore space (that is, the presence of water).

On Line 5 we acquired resistivity data using a 10-channel IRIS Instruments, Inc., Syscal Pro 48©. To cover the entire transect, we spaced 48 stainless steel electrodes on the ground at 10 m intervals to create a 470-m-long line and used a dipole-dipole array with fixed 10 m spacing between the current and voltage electrodes. To improve subsurface resolution, we added measuring points by varying the distance between the current and voltage electrode pairs from one to 10 times the electrode spacing (i.e. 10–100 m). We acquired 710 measurements, with a modeled maximum investigation depth of about 120 m based on theoretical relationships between electrode spacing and geometry and investigation depth for a homogeneous earth medium (e.g. Loke, 2004). Time constraints in the field prohibited reciprocal measurements. Instead, we quantified noise levels using repeatability tests and edited data from Line 5 to remove outliers and negative or zero apparent resistivity values. This reduced the dataset by approximately 28%.

The objective of resistivity inversion is to find a resistivity model that provides a set of theoretical measurements (forward response) that fit the measured data to some pre-described acceptable level (e.g. LaBrecque and Ward, 1990; Oldenburg and Li, 1999; Loke *et al.*, 2003; Günther *et al.*, 2006). If *a priori* information about the subsurface is unavailable, then a smoothness-constraint inversion is utilized to produce smooth models. However, this regularization constraint is conceptually inappropriate when the depths of sharp resistivity contrasts are desired, as is

the case here, where quantifying the depth to highly resistive, fresh bedrock is a goal. If *a priori* subsurface data from geological logs or other geophysical methods are available, alternatives to smoothness-constraint inversion may be used to define layers with sharply contrasting resistivity. For example, in disconnect inversion (Slater and Binley, 2006), the inversion solves for a smoothly varying model structure above and below the resistivity boundary (that is, the 'disconnect') without smoothing across it.

We inverted Line 5 data using both a standard smoothness-constraint inversion and a disconnect-inversion approach using DC2DInvRes (Günther, 2005). The convergence criterion is based on the assumption that the normalized $\chi^2$ equals one if the data are appropriately weighted, given the actual noise and data noise are normally distributed (Johnson *et al.*, 2012), where $\chi^2$ is calculated using Equation (1).

$$\chi^2 = \frac{1}{N_d - 1}\sum_{i=1}^{N_d}\left(\frac{d_{pred,i} - d_{obs,i}}{\sigma_i}\right)^2 \quad (1)$$

Here $N_d$ is the number of measurements, $d_{pred}$ is the predicted data, $d_{obs}$ is the measured data, and $\sigma_i$ is the standard deviation of the measured data. In our inversions, $\chi^2$ equals one when we assume that the data are contaminated with 4% noise. The discretized model space of the foreground region (that is, the area encompassed by the electrode array) contains 2350 cells (a 94 by 25 mesh). We set horizontal cell dimensions at 5 m, equal to one half the electrode spacing, whereas vertical dimensions of cells varied logarithmically from 0 to 130 m. To assess how well our model cells are controlled by the measured data as opposed to model constraints, the sum of absolute sensitivities of all data points are combined and displayed in Figure 7A (following Günther *et al.*, 2003). The results of the sensitivity analysis indicate that the maximum depth of investigation at which the model cells are controlled by the data is about 90 m. As expected, the sensitivities are very low near the model boundaries. To explore this more, we inverted Line 5 data using two different homogenous initial models of 2000 ohm m and 5000 ohm m. The resulting models show consistent spatial distributions of resistivity within the subsurface up to a depth of 90 m, particularly in the high resistivity zone (Figures 7B and 7C).

Figure 8A shows the result of inverting the Line 5 data using the smoothness-constraint inversion method. The inverted model displays a wide range of resistivity values. Resistivity ranges from 500,000 to 25,000 ohm m and is generally higher ($> 10^4$ ohm m) beneath the ridge on the south side of the profile than beneath the swampy meadow to the north ($< 10^4$ ohm m). As expected, due to the effects of using the smoothness constraint, the high and low resistivity zones within the model space have smeared boundaries, which make it difficult to decide if those boundaries are real or simply a result of the employed inversion approach. Regolith with low resistivity is relatively thin (10 m or less) on the hillslope and thickens abruptly to $> 30$ m near the base of the hill and stays deep throughout the meadow, where the upper ~40 m is marked by low resistivity values and strong lateral variations. Generally, the inferred seismic velocity contours (Figure 5A) follow the lateral changes in resistivity, particularly beneath the ridge. However, since the smoothness-based inversion smears out layer boundaries, accurate comparison between velocity and resistivity across the model space is not reliable. To obtain a simplified model (with few resistivity structures) based on Figure 8A, we performed hierarchical clustering, which is based on the magnitude, horizontal location and depth of each model cell (e.g. Defays, 1977; Günther, 2005). The cluster analysis indicates that the model space consists of four clusters, each having different resistivity values (Figure 8B). The high resistivity zone

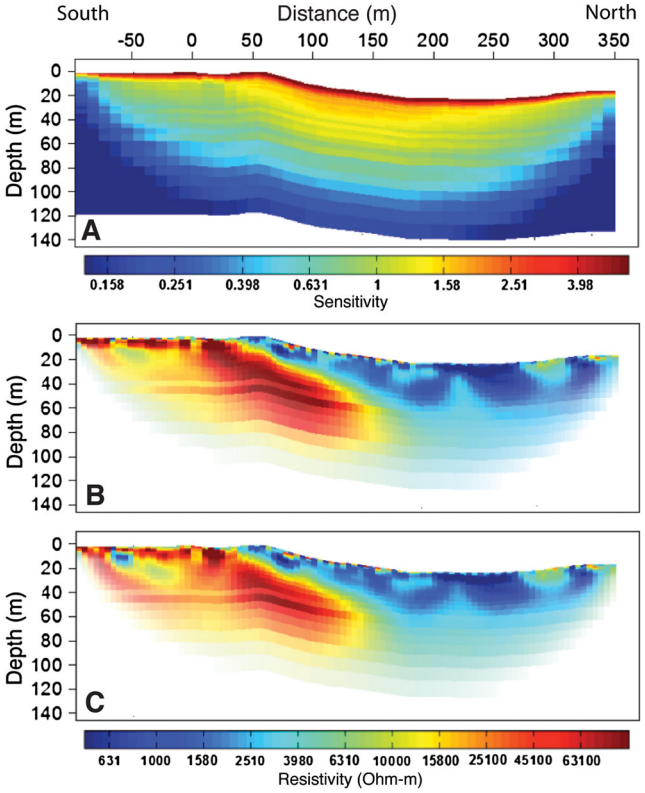


**Figure 7.** Results of the sensitivity analysis. (A) Sensitivity model, (B) smooth inversion model assuming 2000 ohm m homogenous initial model and (C) smooth inversion model assuming 5000 ohm m homogenous initial model. This figure is available in colour online at wileyonlinelibrary.com/journal/espl

beneath the ridge is portioned into two clusters, a result which fits fairly well with the seismic contours at this location. However, the meadow area is portioned into three clusters with different geometries. Unlike under the ridge, the velocity contours under the meadow do not always closely follow inferred resistivity changes.

To obtain an improved estimate of the resistivity distribution above and below the fresh granite bedrock, we inverted the data using the disconnect-inversion approach by incorporating a boundary in the regularization based on the 4 km s$^{-1}$ velocity contour. The disconnect-inversion yields somewhat sharper resistivity boundaries (Figure 8C versus Figure 8A) and an improved match between the seismic contours and the resistivity boundaries, especially beneath the meadow, where the low-resistivity body (~900 ohm m) is bounded at its base by the 4 km s$^{-1}$ velocity contour. The cluster analysis for the disconnect-inversion model (Figure 8D) shows that the resistivity data can be roughly fit (39% RMS error) with only a few major bodies, including (1) a core of high resistivity (~19 000 ohm m) that lies mostly beneath the 4 km s$^{-1}$ contour beneath the hilltop and slope, (2) a surrounding rim of moderately high resistivity (~7000 ohm m), and (3) relatively low-resistivity (~900 ohm m) bodies that extend from the shallow portions of the hillslope to 30 m beneath the meadow. The RMS data misfits for the smoothness-constraint inversion and its associated cluster analysis are 8.4% and 36.8%, respectively. Similarly, RMS misfits are 8.3% and 39.2% for the disconnect inversion and its associated cluster analysis. The forward response of the inverted models fits well with the observed data except at a few spots that have low data coverage (Figure 9). As expected, the cluster analysis models have higher RMS error than the smooth and disconnect inversion approach, since the model space is constrained to a few model parameters, limiting the minimization of data misfit.

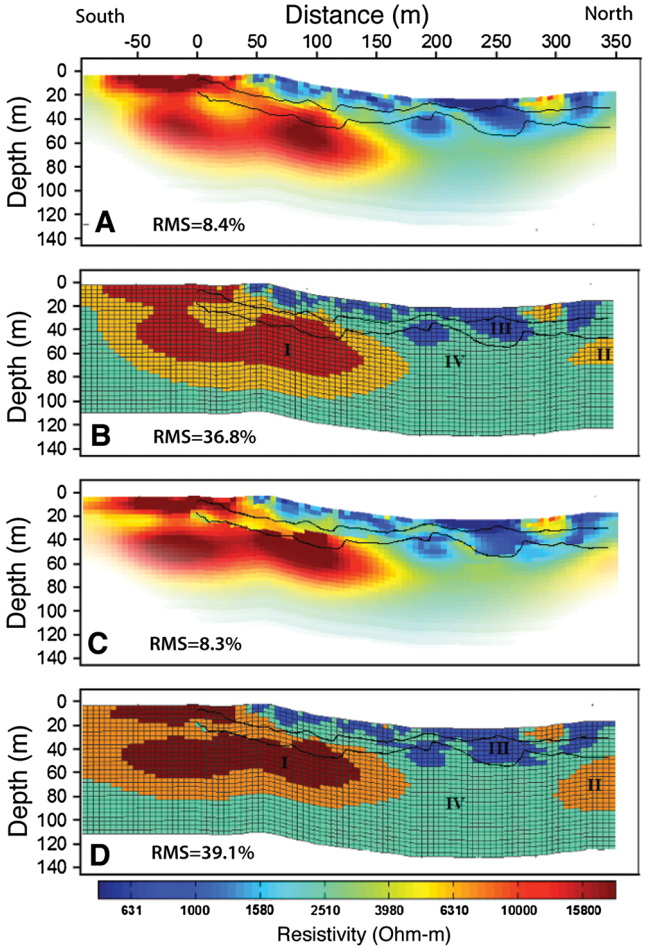


**Figure 8.** Inversion results of Line 5 data (A) smooth inversion, (B) cluster analysis based on the resistivity model in 'A', (C) disconnect inversion, and (D) cluster analysis based on the resistivity model in 'C'. Lines show locations of the 2 and 4 km s$^{-1}$ velocity contours within the resistivity model space. Note that all images have the same color scale. This figure is available in colour online at wileyonlinelibrary.com/journal/espl

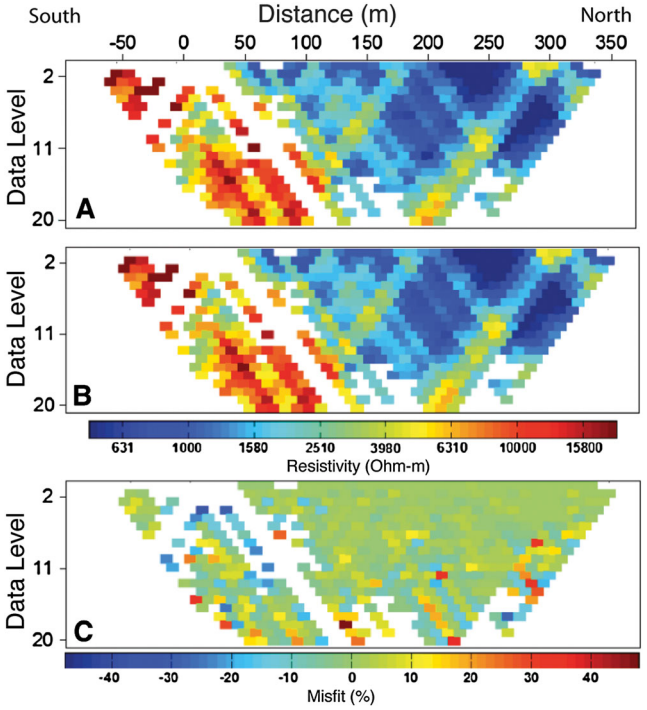


**Figure 9.** Data misfit for the smoothness constraint inversion model. (A) Observed data, (B) predicted data and (C) misfit between the observed and predicted data. The predicted data is consistent with the observed data except at areas of low data coverage. This figure is available in colour online at wileyonlinelibrary.com/journal/espl

For the purposes of comparison to the seismic model and geological interpretation, discussed later in the paper, we use the disconnect model of Figure 8C as our preferred model.

## Bulk density and porosity

To put additional constraints on variations in subsurface weathering across the site, we measured saprolite porosity ($\varphi$), that is, its volumetric water-storage capacity, on samples collected using both hand augers and Geoprobe® coring. Hand auger samples were collected from depths of 30 to 540 cm by augering into saprolite at five locations within a 5 m radius of CZT-1, located near the crest of the ridge spanned by Line 5 (Figure 2B and Table I). We also augered into the subsurface and collected samples at two additional points along Line 5. Together, our regolith augered samples provide an independent check on geophysics-based estimates of subsurface porosity (as discussed later). All augered samples were collected coincident with the geophysical surveys, in September and October, 2011. At each point, we first hand augered a hole to just above the target sampling depth, and then drove a cylinder of known volume into the underlying saprolite using a slide-hammer attachment on either a Madera© sampler (for shallow depths) or an AMS© sampler (for deeper depths). To minimize compaction that might be induced by the hammer, we used marks on the sampler as a gauge on when to stop driving the cylinder.

In September 2012, additional volumetric soil samples were collected from five boreholes along the geophysical transect down to a maximum depth of 11.5 m, using a Geoprobe 6610DT, direct push dual speed auger. Samples were collected and sealed in the field in clear plastic sleeves. One-meter core sections were augured at a time and each core was labeled and logged in the field for visual changes in soil type and water content. The core sections were sealed in the field with vinyl end caps and parafilm to prevent moisture loss. In the laboratory, each 1 m section was subsampled in 10 cm increments. Volumetric samples were weighed in the laboratory and placed in an oven to dry for a 24 hour period at 105 °C (Flint and Flint, 2002). After 24 hours, the samples were weighed to obtain an accurate dry soil mass for calculation of the samples' bulk density ($\rho_b$) and volumetric water content. While use of the Geoprobe limits the sample compaction, the use of the hammer, especially at shallow depths, can lead to some compaction. Measured bulk density was corrected for compaction based on the amount of core recovered per 1 m pushed. The maximum depth was determined by the rejection depth of the geoprobe. Here we use samples from hole CZG-1, which was located near the ridge at tree CZT-1.

Porosity of both hand-auger and Geoprobe samples was estimated as:

$$\varphi = 1 - {}^{\rho_b}/_{\rho_s} \tag{2}$$

where $\rho_s$ is the particle density, here assumed to be 2.65 g cm$^{-3}$ (Flint and Flint, 2002). We measured the mass of each sample in both the field and laboratory before oven drying them for 24 hours at 105 °C (Flint and Flint, 2002). We weighed the samples again after allowing samples to cool (thus minimizing effects of convection) for estimates of dry soil mass, which in turn enables calculation of bulk density (based on the known cylinder volume), used here in Equation (2) to estimate porosity. Saturation, the percent of pore volume occupied by water, was

**Table I.** Mean bulk density and porosity values with standard deviations ($\sigma$, calculated where possible) for hand-auger and geoprobe samples used in this paper.

| | | $g\,cm^{-3}$ | | $cm^3\,cm^{-3}$ | | $cm^3\,cm^{-3}$ | | |
|---|---|---|---|---|---|---|---|---|
| Soil Depth (m) | Type | Mean $\rho_b$ | σ | Mean $\phi$ | σ | Mean VWC | σ | % Saturation |
| 0.3 | Auger | 1.27 | 0.14 | 0.52 | 0.05 | 0.13 | 0.05 | 0.25 |
| 0.6 | Auger | 1.43 | 0.18 | 0.46 | 0.07 | 0.11 | 0.01 | 0.24 |
| 0.75 | Auger | 1.30 | | 0.51 | | 0.11 | | 0.22 |
| 0.9 | Auger | 1.39 | 0.15 | 0.48 | 0.06 | 0.12 | 0.02 | 0.25 |
| 1.2 | Auger | 1.51 | 0.07 | 0.43 | 0.03 | 0.15 | 0.03 | 0.34 |
| 1.5 | Auger | 1.52 | 0.13 | 0.43 | 0.05 | 0.16 | 0.04 | 0.38 |
| 1.8 | Auger | 1.44 | 0.10 | 0.46 | 0.04 | 0.18 | 0.01 | 0.40 |
| 2 | Auger | 1.44 | 0.17 | 0.46 | 0.07 | 0.14 | 0.05 | 0.31 |
| 0.7 | Geoprobe | 0.96 | | 0.64 | | 0.07 | | 0.12 |
| 1.7 | Geoprobe | 1.28 | | 0.52 | | 0.12 | | 0.23 |
| 2.7 | Geoprobe | 1.27 | | 0.52 | | 0.13 | | 0.25 |
| 3.7 | Geoprobe | 1.12 | | 0.58 | | 0.16 | | 0.28 |
| 4.7 | Geoprobe | 1.35 | | 0.49 | | 0.18 | | 0.38 |
| 5.7 | Geoprobe | 1.36 | | 0.49 | | 0.17 | | 0.35 |
| 6.7 | Geoprobe | 1.38 | | 0.48 | | 0.19 | | 0.40 |
| 7.7 | Geoprobe | 1.49 | | 0.44 | | 0.21 | | 0.48 |
| 8.7 | Geoprobe | 1.58 | | 0.40 | | 0.27 | | 0.67 |
| 9.7 | Geoprobe | 1.72 | | 0.35 | | 0.35 | | 0.99 |
| 10.2 | Geoprobe | 1.64 | | 0.38 | | 0.33 | | 0.87 |

Note: VWC = volumetric water content = water filled porosity; saturation = percent of pore space occupied by water.

calculated as the volumetric water content divided by porosity. Results for our porosity measurements are shown in Table I. Porosity ranges from 0.35 to 0.64, with higher values generally near the surface.

## Discussion

### Weathering timescales

The geophysical estimates of regolith thickness from Line 5 range from ~10 to 35 m (Figure 5B). How long does it take to develop a weathering profile that thick? Or, more appropriately, given that the regolith is eroding, what is the average residence time of regolith on the landscape? To find out, we simply divide regolith thickness by an estimate of its overall erosion rate, or equivalently (assuming steady-state thickness), by the regolith production rate. Although regolith production rates are not easy to measure (Dosseto *et al.*, 2008), cosmogenic nuclides average erosion rates over millennial timescales and thus can be used to roughly approximate regolith residence times. *In situ*-produced cosmogenic beryllium-10 ($^{10}$Be) in saprolite from a slope on the edge of P301 (Dixon *et al.*, 2009) yield the most proximal estimate for our purposes. The overall denudation rate (including both chemical and physical erosion) for the slope is reportedly $220\,t\,km^{-2}\,yr^{-1}$ (Dixon *et al.*, 2009), near the middle of the factor of ~10 range of denudation rates implied by cosmogenic nuclides in stream sediment from elsewhere in the Sierra Nevada (Riebe *et al.*, 2000, 2004). It is also broadly consistent with the $\sim 0.3\,m\,Ma^{-1}$ regional average rate of river incision (equivalent $\sim 80\,t\,km^{-2}\,yr^{-1}$ of landscape erosion), which has evidently persisted for the last ~1 Ma, according to cosmogenic burial dating of cave sediment in the region (Stock *et al.*, 2004).

To obtain regolith residence times, we first convert thickness to mass using the average density of subsurface samples reported in Table I (i.e. $\sim 1.40\,g\,cm^{-3}$). We then divide the range in masses by the erosion rate ($220\,t\,km^{-2}\,yr^{-1}$) and calculate 64–220 ka as a plausible range of regolith residence times. Thus soils found at the surface today in the SSCZO evidently reflect the integration of subsurface weathering and erosion over $10^5$-yr timescales. This suggests that regolith properties and structure we see in our geophysical surveys may be relicts of past conditions that were very different from those that drive weathering and erosion today. Although incision rates of master drainages in the region have apparently been fairly stable over the estimated range of residence times (Stock *et al.*, 2004), the streams surrounding the SSCZO are marked by pronounced knickpoints (Wahrhaftig, 1965), consistent with waves of incision propagating through the landscape. Even if base-level lowering rates have been roughly steady, climate has fluctuated markedly in the region over the last 100–200 ka (e.g. Oster *et al.*, 2009). Although the SSCZO lies outside of the mapped limits of Pleistocene glaciation (Gillespie and Zehfuss, 2004), it is high enough that it was likely influenced during glacial intervals by peri-glacial processes, which could have affected erosion and subsurface weathering. In addition, any variations in temperature and moisture over time might have influenced the instantaneous weathering rate; one implication of this may be that long-term averages measured by geochemical mass-balance techniques (e.g. Riebe *et al.*, 2004; Dixon *et al.*, 2009; Rasmussen *et al.*, 2011) do not strongly reflect effects of current climatic conditions.

The long residence times and possible influence of climate change on regolith at the SSCZO raise doubts about whether outputs from erosion are balanced by inputs from regolith production (Figure 1) over the timescales of regolith formation. If not, then the thickness and possibly also properties of regolith have been changing and the system is not in geomorphic steady state. Similar doubts surfaced in an intensive study of subsurface well logs and cosmogenic nuclides in granites of the Colorado Front Range (Dethier and Lazarus, 2006), in what is now the Boulder Creek CZ Observatory. In contrast, at the Luquillo CZ Observatory, in tropical Puerto Rico, the consistency among rates of weathering and erosion over diverse timescales (White *et al.*, 1998; Riebe *et al.*, 2003; Buss *et al.*, 2008; Ferrier *et al.*, 2010) has been interpreted to imply that regolith developed in quartz diorite bedrock is in geomorphic steady state (Chabaux *et al.*, 2013).

## Porosity in saprolite

Seismic velocity in saprolite is lower than in unweathered granite for two reasons: increased porosity due to weathering, and the replacement of minerals such as feldspars with lower-velocity clays (e.g. Olona *et al.*, 2010). We can estimate the porosity distribution in the subsurface from our seismic velocity models by predicting the velocity of a mineral aggregate over a range of possible porosities and finding the porosities that best match the observed velocities. Since modeled porosity depends on the degree of saturation of pores, we calculate two end-member estimates of porosity, one for dry porosity and one for saturation. The dry porosity model provides a minimum estimate of porosity, since fully saturated rocks have higher velocities than dry rocks and thus a higher potential porosity than dry rocks of equal velocity (e.g. Mavko and Mukerji, 1998). We then compare our predicted porosity models to porosity and saturation values measured from the auger and geoprobe core samples near CZT-1. As shown later, the core samples match the minimum (dry)-porosity model in the upper few meters of the subsurface and approach the saturated-porosity model near the base of the saprolite (~10 m).

We predict seismic velocity as a function of porosity and mineralogy with a rock physics model based on Hertz–Mindlin contact theory (Mindlin, 1949), as formulated by Helgerud (2001) and Helgerud *et al.* (1999). This approach treats regolith and rock as aggregates of randomly packed spherical grains and expresses their bulk elastic properties (bulk modulus, $K$, and shear modulus, $G$) as functions of effective pressure, porosity, the elastic properties of constituent minerals, and a critical porosity ($\varphi_c$) above which the aggregate changes from a suspension to a grain-supported material (typically 36-40%; Nur *et al.*, 1998). The Hertz–Mindlin theory establishes the effective bulk ($K_{HM}$) and shear ($G_{HM}$) moduli of the dry rock frame at $\varphi_c$ as:

$$K_{HM} = \left[\frac{n^2(1-\varphi_c)^2 G^2}{18\pi^2(1-\nu)^2} P_{eff}\right]^{1/3} \tag{3}$$

$$G_{HM} = \frac{5-4\upsilon}{5(2-\upsilon)}\left[\frac{3n^2(1-\varphi_c)^2 G^2}{2\pi^2(1-\nu)^2} P_{eff}\right]^{1/3} \tag{4}$$

where $\upsilon$ is Poisson's ratio, $(3K-2G)/(6K+2G)$, $n$ is the average number of contacts per grain (we use $n=5$, following Bachrach *et al.*, 2000), and effective pressure, $P_{eff}$, is given by

$$P_{eff} = (\rho_b - \rho_w) g D \tag{5}$$

In Equation (5), $\rho_w$ is the density of water (1000 kg m$^{-3}$), $D$ is the depth below the surface in meters, $g$ is gravitational acceleration (9.8 m s$^{-2}$), and $\rho_b$ is the bulk density, given by

$$\rho_b = \varphi\rho_w + (1-\varphi)\rho_s \tag{6}$$

where $\rho_s$ is the density of the solid mineral constituents (here taken as 2650 kg m$^{-3}$). We assume a $\varphi_c$ of 0.38 and use the modified upper and lower Hashin–Shtrikman bounds (equations (6.4–6.7) of Helgerud, 2001), respectively, to calculate elastic moduli of the dry frame ($K_{dry}$ and $G_{dry}$) above and below $\varphi_c$. Once the bulk and shear moduli ($K$ and $G$) of the medium for a given porosity are calculated, P-wave velocity can be calculated from

$$v_p = \sqrt{\frac{K+\frac{4}{3}G}{\rho_b}} \tag{7}$$

The rock physics model must be applied differently for dry (air-filled) or saturated (water-filled) porosity, as $K$, $G$ and $\rho_b$ in Equation (7) depend on the pore fluid. To model dry porosity, we set $\rho_w = 0$ in Equations (5) and (6), since air has a density of ~0 and the effective pressure for dry saturation depends only on the bulk density of the overlying solid material, and use $K_{dry}$ and $G_{dry}$ and as $K$ and $G$ in Equation (7). For saturated porosity, the bulk modulus is given instead by $K_{sat}$ calculated from Gassmann's (1951) equation:

$$K_{sat} = K_{solid}\frac{\varphi K_{dry} - \frac{(1-\varphi)K_f K_{dry}}{K_{solid}} + K_f}{(1-\varphi)K_f + \varphi K_{solid} - K_f K_{dry}/K_{solid}} \tag{8}$$

We tested the sensitivity of our predicted velocities (and thus porosities) to compositional variations by modeling the elastic properties of the solid frame over a range of 25 to 50% quartz ($K$ = 44 GPa, $G$ = 36.6 GPa), 10–65% feldspar ($K$ = 70 GPa, $G$ = 30 GPa), and 0–65% clay ($K$ = 20.9 GPa, $G$ = 6.85 GPa), which simulates effects of a large range in degree of weathering of feldspars to clays (elastic constants from Helgerud *et al.* (1999) and Bass (1995)). These minerals typically dominate regolith in granite weathering profiles (Dahlgren *et al.*, 1997); variations in the abundance of other primary and secondary minerals (for example, hornblende) will not significantly affect the predicted velocities. Bulk solid elastic constants were calculated using the averaging formula of Hill (1952). We create a porosity model by varying porosity in Equation (6) to predict velocities from Equation (7), then comparing with the tomographic velocity model to find the best-fitting porosity at each point in the subsurface.

A minimum (dry)-porosity model calculated in this way, assuming a mineralogy of 50% feldspar, 25% quartz, and 25% clay, shows that substantial porosity exists in the saprolite beneath much of the surface on Line 5 (Figure 10), consistent with weathering that is both extensive and deep. Predicted porosities are about 0.4 ± 0.1 at the surface, decreasing with depth to zero at around 25–30 m depth (shallower in places). On average beneath the hillslope, minimum porosity is 0.2 or higher in the upper ~8 m. Subsurface weathering at the hilltop around the heavily instrumented white fir (CZT-1) is particularly extensive and deep, with minimum porosities of 0.2 extending down to about 10 m depth and 0.05 down to 15 m depth. Uncertainties in modeled porosity due to potential mineralogical variability are about ±0.1 at the surface and decline substantially with depth. We note that the predicted velocity at zero porosity for compositions considered here is about 4.2 km s$^{-1}$, close to the 4.0 km s$^{-1}$ observed on the granite outcrop; this suggests that our porosity model is calibrated to within ±0.05, at least at the low-porosity end.

Samples of saprolite from hand augering and geoprobe coring near CZT-1 provide an important check on our porosity model and indicate the critical role of pore saturation in creating porosity models from seismic velocities. Measured porosity values in the upper few meters are high (~40–50%), consistent with porosities predicted by our minimum-porosity model (Figure 10). However, at depths greater than ~3 m, sample porosities diverge from the model, staying well above the minimum-porosity model down to depths of 10 m. The explanation for this lies in the observed saturation values of the samples, which increase from ~15–20% in the upper 2 m to nearly ~90% at 10 m depth (Table I). As saturation increases with depth, the observed porosity values approach the saturated-porosity model, as expected (Figure 10B). This comparison indicates that our minimum-porosity model produces reasonable estimates where pore space is dry but may significantly underestimate total porosity in water-saturated settings.

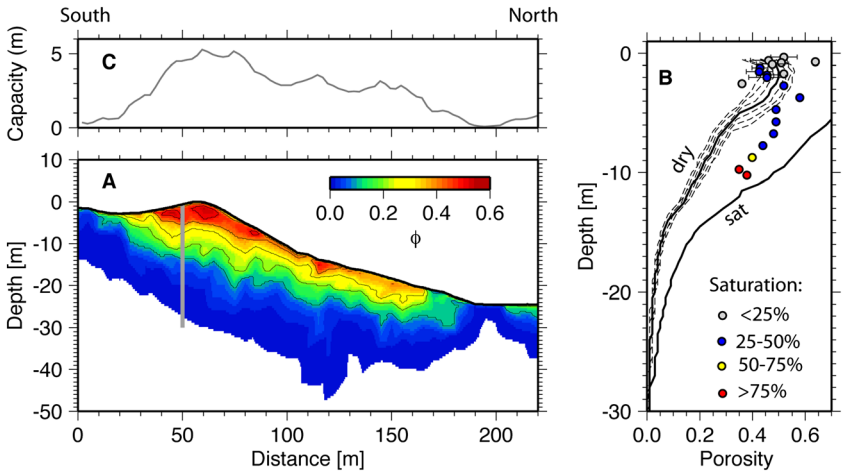


**Figure 10.** Interpretation of geophysical data and analysis of bulk samples from Line 5. (A) Porosity model on southern portion of Line 5, calculated from seismic velocities using a rock physics model, and assuming dry porosity and a composition of 50% feldspar, 25% quartz, and 25% clay. Porosity is contoured every 0.1 (10%). These are minimum values for porosity for this composition; if pore space is saturated, higher porosities would be needed to match seismic velocities. White region at base shows area where porosity is predicted to be zero (that is, at the bedrock–regolith interface). (B) Predicted porosity–depth profiles at the location of the gray line in A, near the white fir CZT-1, for dry porosity ('dry') and water-saturated porosity ('sat'). Solid lines show the predicted porosity for the composition assumed in A; dashed lines show sensitivity of porosity calculation to variation in composition over a range 25–50% quartz, 10–65% feldspar, and 0–65% clay (shown only for dry porosity model). Circles mark porosities (± standard deviations where available) measured from volumetric samples of saprolite (see text), color-coded by measured saturation values (Table I) as indicated in legend. The minimum-porosity model provides good agreement with measured porosities in the upper 3 m, where porosity is mostly dry. At deeper depths, porosities are closer to the saturated model, as expected given the increase in measured saturation of samples with depth. (C) Total water storage capacity of the subsurface, in meters of water, calculated by integrating porosity profiles with depth at all positions across the model. At the top of the hill near CZT-1, the subsurface could hold a minimum of ~5 $m^3\,m^{-2}$ of water if fully saturated; over the entire profile, the minimum water holding capacity averages ~3 $m^3\,m^{-2}$. This figure is available in colour online at wileyonlinelibrary.com/journal/espl

## Comparison of seismic velocity and resistivity

Because seismic velocity and resistivity are sensitive to different physical properties, a comparison between them can enhance insight into subsurface structure and water content (Figure 8). Here we compare the resistivity model obtained from the disconnect-inversion approach with the seismic velocity model, as this approach is conceptually consistent with the expected resistivity transition from regolith to unweathered bedrock. High resistivities ($> 10^4$ ohm m) reach the surface just south of the hilltop, where bedrock crops out, consistent with the expected high resistivity of granite ($> 10^4$ ohm m; [Olhoeft, 1981]). Velocities there are nearly 2 $km\,s^{-1}$ at the surface. The underlying 4 $km\,s^{-1}$ contour, which likely marks the transition from moderately to unweathered bedrock (as described later), approximately follows the transition between moderate (~7000 ohm m) and high (~19 000 ohm m) resistivities. Beneath the upper hillslope ($x = 70$–$150$ m), the upper ~15 m of the subsurface has velocities $< 2.0$ $km\,s^{-1}$ (probably encompassing saprolite, as discussed later) and lower resistivity values ($< 10^3$ ohm m) that likely indicate the presence of clay and/or small amounts of water.

Several zones of low resistivity (< 1000 ohm m) exist in the model beneath the hillslope and meadow. The lowest resistivities (< 600 ohm m) form a northward-dipping, highly conductive body in the uppermost 5–10 m beneath the meadow ($x = 220$–$270$ m in Figure 8). Resistivity in rocks and soils is strongly dependent on porosity, pore saturation and pore fluid content, as water is typically much less resistive than minerals (e.g. Samouëlian *et al.*, 2005); electrical conductivity due to water in soils increases rapidly as saturation increases from adsorbed water in the vadose zone to free water in pores (e.g. Saarenketo, 1998). The conductive body in the meadow very likely corresponds to the water table; the meadow itself was water-logged and marshy at the surface during the survey. Alternatively (or additionally), low resistivity could indicate the presence of clays, which enhance conductivity (Samouëlian *et al.*, 2005). Whether the low-resistivity bodies indicate the presence of water or clay (or both), they are likely linked to coupled weathering and hydrological processes, since water is a major agent for bedrock weathering. In the disconnect inversion, the 4 $km\,s^{-1}$ contour corresponds nearly everywhere to a downward increase in resistivity, suggesting that it may correspond to the boundary between weathered and nearly intact bedrock. The one exception is a deeper pocket of low resistivity just beneath the 4 $km\,s^{-1}$ contour under the southern edge of the meadow ($x \sim 200$ m), possibly indicating a locally saturated zone within the bedrock.

All inversion results show a strong lateral change in bedrock resistivity beneath the 4 $km\,s^{-1}$ contour, from highly resistive rock (~19 000 ohm m) beneath the upper hillslope to much less resistive (~2000 ohm m) beneath the lower hillslope and meadow (for example, the transition from units I to II to IV in Figure 8D). The most likely explanation for this change is a contrast in the saturation of pore spaces (microporosity and/or fracture porosity) in the bedrock, from dry porosity at the top of the hillslope to saturated conditions beneath the lower hillslope and meadow. Alternatively the phenomenon could reflect precipitation of clays in the meadow from leaching of regolith on the slope (e.g. Yoo *et al.*, 2009). The downslope enrichment of clay would appear as a decrease in resistivity, which might be abrupt, at the forest-meadow transition, if illuviation is driven by reducing conditions associated with the more continuous presence of water in the meadow. The corresponding change in seismic velocities might be less pronounced due to their lower sensitivity to clay content (Figure 10B). Drilling and sampling of the subsurface in the region near the meadow would help test this hypothesis.

## Conceptual model

The coupled seismic and resistivity data presented here offer unique insights into the subsurface structure and water content of the SSCZO and thus provide a basis for generating a

conceptual model of the CZ (Figure 11). The model has two main features relating to weathering (primarily inferred from seismic velocities and porosities) and pore saturation (primarily inferred from resistivity values). First, a vertical gradient in weathering is indicated by the increasing seismic velocities (and inferred porosity decrease) with depth. Beneath a thin soil layer (which is assumed but not resolved in our geophysical images), we interpret three main physically intact subsurface layers: saprolite, moderately weathered bedrock, and unweathered bedrock. Second, a lateral change in pore saturation (and/or clay content) is suggested by the strong lateral change in resistivity from the hillslope to the meadow. Later we describe the basis for the interpretive cross-section (Figure 11) in detail.

Saprolite is defined here as the sub-soil unit where velocities are less than 2 km s$^{-1}$. Beneath the hillslope on our model, the 2 km s$^{-1}$ contour closely coincides with a major downward increase in resistivity, from < 1000 to > 5000 ohm m, suggesting that, in the relatively 'dry' (electrically resistive) hillslope environment, the 2 km s$^{-1}$ contour marks a significant physical transition. The porosity model (Figure 10) provides further support for this interpretation: at the depths with $V = 2$ km s$^{-1}$, (~20 m at $x = 50$ m) porosity is only 5–10%, much lower than typical saprolite porosities (> 20%, e.g. Driese *et al.*, 2001). Several previous studies of velocities in weathered granite support choosing the 2 km s$^{-1}$ contour as a threshold between saprolite and moderately weathered bedrock (Begonha and Braga, 2002; Olona *et al.*, 2010). Begonha and Braga (2002) measured seismic velocities on weathered granite and saprolite samples from the Oporto granite (Portugal) and found a close correlation between the degree of weathering, seismic velocity and porosity and identified porosity as the physical property most strongly influenced by weathering. They measured ultrasonic velocities on 167 drill core samples; 2.0 km s$^{-1}$ marks the boundary between samples characterized as weathering grade W3 ('weathered rock') and W3–W4, which includes saprolite. Olona *et al.* (2010) conducted a comprehensive study of the elastic (Vp, Vs) and electrical properties of a weathering granite terrain in northwest Spain. Their study included ground-truthing from a 35-m-deep borehole and laboratory measurements of density, porosity, and ultrasonic velocity. The boundary between granite

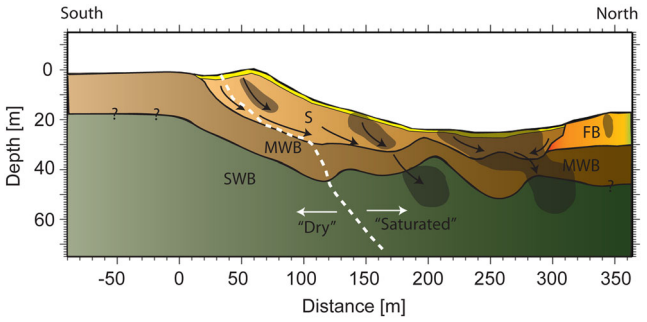


**Figure 11.** Interpretive cross section of Line 5, based on seismic velocity and resistivity data. Vertical stratification based primarily on seismic velocities (Vp) and are approximate depths of more gradational transitions between saprolite (S, Vp < 2 km s$^{-1}$), moderately weathered bedrock (MWB, 2 km s$^{-1}$ Vp < 4 km s$^{-1}$), and more-or-less unweathered bedrock (UB, Vp > 4 km s$^{-1}$). White dashed line shows approximate boundary at the time of our survey between dominantly unsaturated pore space ('dry') and largely saturated pore space, as indicated by the lateral transition from high to low resistivity (Figure 8). FB is a fractured bedrock unit exposed on the surface, which has low Vp but high resistivity. Gray zones are locations of highly conductive (< 500 ohm m) bodies resolved in the resistivity model. Black arrows show speculative sense of subsurface water flow. The symbols '?' denote locations where interpretation is based on resistivity data alone. This figure is available in colour online at wileyonlinelibrary.com/journal/espl

'fully or partially weathered to soil,' with a rock quality designation (i.e. RQD after Deere, 1964) of 17%, and 'fresh rock,' with an RQD of > 50%, corresponds to an increase in P-velocity from 1.45 to 2.6 km s$^{-1}$. These lines of evidence all point to 2 km s$^{-1}$ as a good proxy for the boundary between saprolite and underlying moderately weathered bedrock.

The transition from moderately weathered to virtually intact basement likely takes place near the 4 km s$^{-1}$ isovelocity contour. Several lines of evidence support this interpretation. First, seismic data from Line 9 (Figures 3–5) show that intact bedrock exposed in an extensive surface outcrop has a seismic velocity of 4 km s$^{-1}$. While this bedrock is not pristine – it shows several macroscopic fractures and some biotite staining – it is intact and is only slightly weathered. This outcrop thus provides direct 'ground truth' that 4 km s$^{-1}$ corresponds to virtually unweathered bedrock in our study area. Second, the rock physics model presented earlier predicts a velocity of 4.2 km s$^{-1}$ for zero porosity at the low confining pressures of our study area for the mineralogies assumed here. Hence, a velocity of 4.0 km s$^{-1}$ indicates, on average, low porosities (< 0.01), consistent with only slightly weathered bedrock. (In some places, low resistivity zones beneath the 4.0 km s$^{-1}$ contour may indicate local, fluid-filled fracture zones that are too narrow to resolve with traveltime tomography.) Finally, comparison to other seismic and borehole studies of weathered granite indicates that 4.0 km s$^{-1}$ corresponds to slightly weathered (Begonha and Braga, 2002) or 'fresh' rock (Olona *et al.*, 2010).

The conceptual model in Figure 11 provides a glimpse of the thicknesses of saprolite and weathered bedrock in the SSCZO. The thickness of regolith (defined for our purposes as the soil plus saprolite plus moderately weathered bedrock) ranges from ~10 to 35 m (average = 23 m), with the thickest regolith on the ridge (beneath CZT-1) and the thinnest regolith at the base of the hillslope, just south of the swampy meadow (Figure 5B). Meanwhile, saprolite thickness ranges from near zero at the base of the hillslope to about 20 m near CZT-1. These thicknesses are broadly consistent with studies of saprolite development elsewhere in granites of the southern Sierra Nevada (Graham *et al.*, 2010) and with our own general observations of weathering profiles in roadcuts in the region.

At the north end of the seismic and resistivity surveys on Line 5, a blocky bedrock outcrop was crossed ('fractured bedrock,' FB, in the interpretive cross-section; Figure 11). The granite there appears as a resistive block on the resistivity model ($x = 270$–$310$ m, Figure 8), but the surface layer of the seismic velocity model there shows low velocities (< 1 km s$^{-1}$). The low seismic velocities here (which are resolved by travel times recorded by the end shotpoint; Figure 4) must therefore indicate that pervasive fracturing of the surface bedrock has lowered seismic velocities to be indistinguishable from saprolite. Alternatively, the block of rock, while evident at the surface, may be too small to be fully resolved as a 4 km s$^{-1}$ anomaly by the seismic survey. The high resistivity of this zone suggests that the fracture porosity was unsaturated, consistent with drainage of residual moisture from the slope by the time of our survey, in October (that is, long after the last of the previous winter's snow melted from the site).

Our conceptual model includes speculations on possible subsurface water flow paths (arrows, Figure 11). In hard rock terrain, weathering exerts a major control on hydrogeology. Porosity is primarily a function of degree of weathering (e.g. Begonha and Braga, 2002), whereas connectivity and permeability are affected both by porosity and by hydraulic conductivity along fractures (Taylor and Howard, 2000; Dewandel *et al.*, 2006). Permeability is likely to be anisotropic in the presence of fractures (Marechal *et al.*, 2003); significant hydraulic conductivity can persist in weathered granite terrain to depths of 35 m, due to intersecting sets of sub-horizontal and sub-

vertical fractures (Marechal *et al.*, 2004). We speculate that subsurface water flow is largely downhill from the vicinity of CZT-1, which was largely dry at the time of our survey, based on resistivity measurements, to the meadow, which was saturated and boggy during our survey, with the water table at the surface. Downslope flow is guided by permeability structure and orientation of weathering zones. In particular, the downslope dip of the base of the saprolite (Figure 11) likely channels flow down toward the meadow. The stark resistivity contrast between the resistive hilltop and more conductive lower meadow may be a permeability phenomenon; we speculate that gravity-driven drainage precludes percolation of water into the low-porosity, weathered bedrock beneath the slope, whereas low hydraulic gradients and ponding in the meadow may permit water to seep more effectively into bedrock cracks. We speculate that the isolated highly conductive zones beneath the meadow may represent areas of recharge or ponding of subsurface water, with possible contributions from conductive clays that precipitate there as by-products of illuviation from weathering upslope. Such conductive bodies may hold important clues about subsurface weathering patterns in the landscape.

There are numerous caveats to the physical, geochemical and hydrological interpretations presented here. First, it is important to keep in mind that the boundaries between layers are likely not sharp; weathering profiles are probably gradational and while sharp fronts may exist in places, the simple structure shown in Figure 11, with sharp boundaries between 'moderately' and unweathered bedrock, or between saprolite and weathered bedrock, is certainly a simplification. Second, our seismic velocity models, like all tomograms, must be viewed as a spatially smoothed version of reality (e.g. Rawlinson *et al.*, 2010). This smoothing is due to limitations in ray coverage, regularization of the inversion algorithm, and seismic wavelength (20 m for a 100 Hz wave traveling at 2000 m $s^{-1}$). As a consequence, we are unable to distinguish between relatively intact corestones and surrounding highly weathered zones. Our tomogram is an average velocity structure that blurs these distinctions. The fractured bedrock (FB) interpreted on Figure 11 is a direct example of the difficulty in distinguishing macroporosity due to fracturing from microporosity due to weathering; similar regions of fractured bedrock in the subsurface could easily be mistaken for saprolite in the seismic models. Third, we lack data on hydraulic head in this watershed, so our suggestions of possible subsurface groundwater flow are purely speculative. While hydraulic head is generally expected to mimic topography, with recharge zones at high elevation and discharge at lower elevation, this may not be true in any given catchment (Winter, 1999). Finally, and most importantly, our geological interpretation is unconstrained by direct sampling via boreholes or outcrops. Nevertheless, we should be able to test the interpretation proposed by Figure 11 in future drilling, sampling, and hydrogeological measurements. The competing hypotheses proposed here arise from the coupling of resistivity and seismic refraction studies; this highlights a benefit of using multiple geophysical approaches in the study of deep CZ architecture and processes.

## Conclusions

We investigated the subsurface architecture of the SSCZO using seismic refraction and electrical resistivity data. Seismic velocity variations provide robust first-order constraints on the distribution of weathering in the subsurface. We find depths of weathering average about 23 m, consistent with roadcuts and other regional studies of deep weathering. Beneath a roughly meter-thick layer of soil, regolith is divided approximately equally between an upper layer of saprolite and a lower layer of moderately weathered bedrock. We coupled our geophysical estimates of regolith thickness with previously published long-term erosion rates and inferred that soils now found at the surface integrate weathering over 100 000-year timescales and thus may reflect the influence of wide fluctuations in climate associated with glacial–interglacial intervals.

We used a rock physics model based on Hertz–Mindlin contact theory to constrain water storage potential in the subsurface. Porosities predicted from a minimum-porosity model decrease from ~50% near the surface to near zero at the base of weathered rock; this is broadly consistent with physical measurements of porosity in samples from the upper 3 m of the subsurface. Porosities measured in deeper (3–10 m) samples are higher than those predicted by the minimum-porosity model and approach the values predicted from a water-saturated porosity model; this is consistent with observed increases in saturation in the samples. These results indicate that seismic velocities can be used to estimate minimum water storage potential in the subsurface. Across the surveyed slope, we estimate that the minimum water storage potential averages ~3 $m^3\,m^{-2}$ and ranges from $< 1$ to 5 $m^3\,m^{-2}$. Our results imply that saprolite and weathered bedrock of the deep CZ may be crucial water storage elements in the SSCZO.

*Acknowledgements*—The authors thank James St Clair, Devin Oderwald, Ryan Lucas, Sayaka Araki, and Barbara Jessup for assistance in the field. Matt Meadows masterfully coordinated field logistics. The authors thank the IRIS/PASSCAL Instrument Center for seismic equipment loan; Geometrics, Inc. for seismic inversion software; Thomas Günther for resistivity inversion software; and Roger Bales and Ye Zhang for helpful conversations. Sayaka Araki helped generate Figure 2. The authors also thank the US Forest Service and Carolyn Hunsaker for access to KREW catchments and for use of the Glen Meadow Work Center as a base station. Finally, the authors thank Arjun Heimsath, an anonymous reviewer, and Stuart Lane for constructive comments on the manuscript. This work was funded by the National Science Foundation, through the National CZO Program (EAR-0725097 and 1239521), the NSF-EPSCoR program (EPS-1208909) and by the University of Wyoming's Marathon Geophysics Field Excellence Fund. This is a publication of the Wyoming Center for Environmental Hydrology and Geophysics and the Southern Sierra CZO.

## References

Anderson SP, Dietrich WE, Brimhall GH. 2002. Weathering profiles, mass-balance analysis, and rates of solute loss: Linkages between weathering and erosion in a small, steep catchment. *Geological Society of America Bulletin* **114**: 1143.

Anderson SP, von Blanckenburg F, White AF. 2007. Physical and chemical controls on the critical zone. *Elements* **3**: 315–319. DOI: 10.2113/gselements.3.5.315

Anderson SP, Bales RC, Duffy CJ. 2008. Critical zone observatories: building a network to advance interdisciplinary study of Earth surface processes. *Mineralogical Magazine* **72**: 7–10. DOI: 10.1180/minmag.2008.072.1.7

Anderson RS, Anderson SP, Tucker GE. 2013. Rock damage and regolith transport by frost: an example of climate modulation of the geomorphology of the critical zone. *Earth Surface Processes and Landforms* **38**(3): 299–316.

Bachrach R, Dvorkin J, Nur AM. 2000. Seismic velocities and Poisson's ratio of shallow unconsolidated sands. *Geophysics* **65**(2): 559–564.

Bales RC, Hopmans JW, O'Geen AT, Meadows M, Hartsough PC, Kirchner P, Hunsaker CT, Beaudette D. 2011. Soil moisture response to snowmelt and rainfall in a Sierra Nevada mixed-conifer forest. *Vadose Zone Journal* **10**: 786–799. DOI: 10.2136/vzj2011.0001

Banfield JF, Barker WW, Welch SA, Taunton A. 1999. Biological impact on mineral dissolution: application of the lichen model to understanding mineral weathering in the rhizosphere. *Proceedings of the National Academy of Science, USA* **96**: 3404–3411.

Bass JD. 1995. Elasticity of minerals, glasses, and melts. In *Handbook of Physical Constants*, Ahrens TJ (ed.). American Geophysical Union: Washington, DC; 45–63.

Bateman PC, Wones DR. 1972. *Geologic Map of the Huntington Lake Quadrangle, Central Sierra Nevada, California*. US Geological Survey: Reston, VA.

Befus KM, Sheehan AF, Leopold M, Anderson SP, Anderson RS. 2011. Seismic constraints on critical zone architecture, Boulder Creek Watershed, Front Range, Colorado. *Vadose Zone Journal* **10**: 915–927. DOI: 10.2136/vzj2010.0108

Begonha A, Braga S. 2002. Weathering of the Oporto granite: geotechnical and physical properties. *Catena* **49**: 57–133.

Beylich AA, Kolstrup E, Linde N, Pedersen LB, Thyrsted T, Gintz D, Dynesius L. 2003. Assessment of chemical denudation rates using hydrological measurements, water chemistry analysis and electromagnetic geophysical data. *Permafrost and Periglacial Processes* **14**: 387–397. DOI: 10.1002/ppp.470

Beylich AA, Kolstrup E, Thyrsted T, Linde N, Pedersen LB, Dynesius L. 2004. Chemical denudation in arctic-alpine Latnjavagge (Swedish Lapland) in relation to regolith as assessed by radio magnetotelluric-geophysical profiles. *Geomorphology* **57**: 303–319. DOI: 10.1016/S0169-555X(03)00162-4

Brantley SL, Megonigal JP, Scatena FN, Balogh-Brunstad Z, Barnes RT, Bruns MA, Van Cappellen P, Dontsova K, Hartnett HE, Hartshorn AS, Heimsath AM, Herndon EM, Jin L, Keller CK, Leake JR, McDowell WH, Meinzer FC, Mozdzer TJ, Petsch S, Pett-Ridge J, Pregitzer KS, Raymond PA, Riebe CS, Shumaker K, Sutton-Grier A, Walter R, Yoo K. 2011. Twelve testable hypotheses on the geobiology of weathering. *Geobiology* **9**: 140–165. DOI: 10.1111/j.1472-4669.2010.00264.x

Braun J-J, Descloitres M, Riotte J, Fleury S, Barbiéro L, Boeglin J-L, Violette A, Lacarce E, Ruiz L, Sekhar M, Mohan Kumar MS, Subramanian S, Dupré B. 2009. Regolith mass balance inferred from combined mineralogical, geochemical and geophysical studies: Mule Hole gneissic watershed, south India. *Geochimica et Cosmochimica Acta* **73**: 935–961.

Burke BC, Heimsath AM, White AF. 2007. Coupling chemical weathering with soil production across soil-mantled landscapes. *Earth Surface Processes and Landforms* **32**(6): 853–873.

Buss HL, Sak PB, Webb SM, Brantley SL. 2008. Weathering of the Rio Blanco quartz diorite, Luquillo Mountains, Puerto Rico: coupling oxidation, dissolution, and fracturing. *Geochimica et Cosmochimica Acta* **72**: 4488–4507. DOI: 10.1016/j.gca.2008.06.020,

Buss HL, Brantley SL, Scatena FN, Bazilievskaya EA, Blum A, Schulz M, Jimenez R, White AF, Rother G, Cole D. 2013. Probing the deep critical zone beneath the Luquillo Experimental Forest, Puerto Rico. *Earth Surface Processes and Landforms* **38**(10): 1170–1186.

Carson MA, Kirkby MJ. 1972. *Hillslope Form and Process*. Cambridge University Press: London; 475 pp.

Chabaux F, Blaes E, Stille P, Roupert RD, Pelt E, Dosseto A, Ma L, Buss HL, Brantley SL. 2013. Regolith formation rate from U-series nuclides: Implications from the study of a spheroidal weathering profile in the Rio Icacos watershed (Puerto Rico). *Geochimica et Cosmochimica Acta* **100**: 73–95.

Clarke BA, Burbank DW. 2011. Quantifying bedrock-fracture patterns within the shallow subsurface: implications for rock mass strength, bedrock landslides, and erodibility. *Journal of Geophysical Research – Earth Surface* **116**: F04009. DOI: 10.1029/2011jf001987

Dahlgren RA, Boettinger JL, Huntington GL, Amundson RG. 1997. Soil development along an elevational transect in the western Sierra Nevada, California. *Geoderma* **78**(3–4): 207–236.

Deere DU. 1964. Technical description of rock cores. *Rock Mechanics and Engineering Geology* **1**: 16–22.

Defays D. 1977. Efficient algorithm for a complete link method. *Computer Journal* **20**(4): 364–366.

Dethier DP, Lazarus ED. 2006. Geomorphic inferences from regolith thickness, chemical denudation and CRN erosion rates near the glacial limit, Boulder Creek catchment and vicinity, Colorado. *Geomorphology* **75**(3–4): 384–399.

Dewandel B, Lachassagne P, Wyns R. 2006. A generalized 3-D geological and hydrogeological conceptual model of granite aquifers controlled by single or multiphase weathering. *Journal of Hydrology* **330**: 260–284. DOI: 10.1016/j.jhydrol.2006.03.026

Dietrich WE, Reiss R, Hsu ML, Montgomery DR. 1995. A process-based model for colluvial soil depth and shallow landsliding using digital elevation data. *Hydrological Processes* **9**(3–4): 383–400.

Dixon JL, Heimsath AM, Amundson R. 2009. The critical role of climate and saprolite weathering in landscape evolution. *Earth Surface Processes and Landforms* **34**: 1507–1521. DOI: 10.1002/esp.1836

Dosseto A, Turner SP, Chappell J. 2008. The evolution of weathering profiles through time: new insights from uranium-series isotopes. *Earth and Planetary Science Letters* **274**: 359–371.

Dosseto A, Buss HL, Suresh PO. 2012. Rapid regolith formation over volcanic bedrock and implications for landscape evolution. *Earth and Planetary Science Letters* **337**: 47–55.

Driese SG, McKay LD, Penfield CP. 2001. Lithologic and pedogenic influences on porosity distribution and groundwater flow in fractured sedimentary saprolite: a new application of environmental sedimentology. *Journal of Sedimentary Research* **71**: 843–1700.

Ferrier KL, Kirchner JW, Riebe CS, Finkel RC. 2010. Mineral-specific chemical weathering rates over millennial timescales: measurements at Rio Icacos, Puerto Rico. *Chemical Geology* **277**(1–2): 101–114.

Flint LE, Flint AL. 2002. Porosity: calculation from particle and bulk densities. In *Methods of Soil Analysis. Part 4: Physical Methods*, Dane JH, Topp GC (eds). Soil Science Society of America: Madison, WI; 241–242.

Gallardo LA, Meju MA. 2003. Characterization of heterogeneous near-surface materials by joint 2D inversion of dc resistivity and seismic data. *Geophysical Research Letters* **30**(13): 1658 1–4.

Gallardo LA, Meju MA. 2004. Joint two-dimensional DC resistivity and seismic travel time inversion with cross-gradients constraints. *Journal of Geophysical Research* **109**(B03311): 1–11.

Gassmann F. 1951. Über die elastizität poröser medien. *Vierteljahrsschrift der Naturforschenden Gesellschaft in Zürich* **96**: 1–23.

Gilbert GK. 1877. *Report on the Geology of the Henry Mountains*. Government Printing Office: Washington, DC; 160 pp.

Gillespie AR, Zehfuss PH. 2004. Glaciations of the Sierra Nevada, California, USA. In *Quaternary Glaciations – Extent and Chronology, Part II*, Ehlers J, Gibbard PL (eds). Elsevier: Amsterdam; 51–62.

Graham R, Rossi A, Hubbert R. 2010. Rock to regolith conversion: producing hospitable substrates for terrestrial ecosystems. *GSA Today* **20**: 4–9.

Günther T. 2005. Inversion Methods and Resolution Analysis for the 2D/3D Reconstruction of Resistivity Structures from DC Measurements, PhD Thesis. University of Mining and Technology, Freiberg.

Günther T, Friedel S, Spitzer K. 2003. Estimation of information content and efficiency for different data sets and inversion schemes using the generalized singular value decomposition. *Proceedings, Electromagnetic Depth Sounding Workshop*, Königstein, Germany.

Günther T, Rucker C, Spitzer K. 2006. 3-d Modeling and inversion of DC resistivity data incorporating topography – part II: inversion. *Geophysical Journal International* **166**: 506–517.

Heimsath AM, Dietrich WE, Nishiizumi K, Finkel RC. 1997. The soil production function and landscape equilibrium. *Nature* **388**: 358–361. DOI: 10.1038/41056

Heimsath AM, DiBiase RA, Whipple KX. 2012. Soil production limits and the transition to bedrock-dominated landscapes. *Nature Geoscience* **5**(3): 210–214.

Heincke B, Guenther T, Dalsegg E, Ronning JS, Ganerod GV, Elvebakk H. 2010. Combined three-dimensional electric and seismic tomography study on the Aknes rockslide in western Norway. *Journal of Applied Geophysics* **70**(4): 292–306.

Helgerud MB. 2001. Wave Speeds in Gas Hydrates and Sediments Containing Gas Hydrate: A Laboratory and Modeling Study, PhD Thesis. Stanford University, Stanford, CA; 249 pp. http://stanford.io/15uCj6B

Helgerud MB, Dvorkin J, Nur A, Sakai A, Collett T. 1999. Elastic-wave velocity in marine sediments with gas hydrates: effective medium modeling. *Geophysical Research Letters* **26**: 2021–2024.

Hill R. 1952. The elastic behavior of crystalline aggregate. *Proceedings of the Physics Society, London* **A65**: 349–354.

Hubbert K, Graham R, Anderson M. 2001. Soil and weathered bedrock: components of a Jeffrey pine plantation substrate. *Soil Science Society of America Journal* **65**: 4.

Hunsaker CT, Eagan SM. 2003. Small stream ecosystem variability in the Sierra Nevada of California. In *Proceedings, First Interagency*

*Conference on Research in the Watersheds*, Renard KG (ed.). USDA-ARS: Washington, DC; 716–721.

Hunsaker CT, Whitaker TW, Bales RC. 2012. Snowmelt runoff and water yield along elevation and temperature gradients in California's Southern Sierra Nevada. *Journal of the American Water Resources Association* 1–12. DOI: 10.1111/j.1752-1688.2012.00641.x

Jessup BS, Hahm WJ, Miller SN, Kirchner JW, Riebe CS. 2011. Landscape response to tipping points in granite weathering: the case of stepped topography in the Southern Sierra Critical Zone Observatory. *Applied Geochemistry* **26**: S48–S50. DOI: 10.1016/j.apgeochem.2011.03.026

Johnson DW, Hunsaker CT, Glass DW, Rau BM, Roath BA. 2011. Carbon and nutrient contents in soils from the Kings River Experimental Watersheds, Sierra Nevada Mountains, California. *Geoderma* **160**: 490–502. DOI: 10.1016/j.geoderma.2010.10.019

Johnson TC, Slater LD, Ntarlagiannis D, Day-Lewis FD, Elwaseif M. 2012. Monitoring groundwater–surface water interaction using time-series and time-frequency analysis of transient three-dimensional electrical resistivity changes. *Water Resources Research*. DOI: 10.1029/2012WR011893.

Knight R, Knight R, Pyrak Nolte LJ, Slater L, Atekwana E, Endres A, Geller J, Lesmes D, Nakagawa S, Revil A, Sharma MM, Straley C. 2010. Geophysics at the interface: response of geophysical properties to solid–fluid, fluid–fluid, and solid–solid interfaces. *Reviews of Geophysics* **48**(RG4002): 1–30.

LaBrecque D, Ward S. 1990. 2-D cross-borehole resistivity model fitting. In *Geotechnical and Environmental Geophysics*, Ward S (ed.). SEG: Tulsa, OK; 51–47.

Landeweert R, Hoffland E, Finlay RD, Kuyper TW, van Breemen N. 2001. Linking plants to rocks: ectomycorrhizal fungi mobilize nutrients from minerals. *Trends in Ecology & Evolution* **16**(5): 248–254.

Lebedeva M, Fletcher R, Brantley S. 2010. A mathematical model for steady state regolith production at constant erosion rate. *Earth Surface Processes and Landforms* **35**: 508–1032. DOI: 10.1002/esp.1954

Lin H, Hopmans JW, Richter DD. 2011. Interdisciplinary sciences in a global network of critical zone observatories. *Vadose Zone Journal* **10**: 781–785. DOI: 10.2136/vzj2011.0084

Loke MH. 2004. 2-D and 3-D Electrical Imaging Surveys. http://www.geoelectrical.com/

Loke MH, Acworth I, Dahlin T. 2003. A comparison of smooth and blocky inversion methods in 2-D electrical imaging surveys. *Exploration Geophysics* **34**: 182–187.

Ma L, Chabaux F, Pelt E, Blaes E, Jin LX, Brantley S. 2010. Regolith production rates calculated with uranium-series isotopes at Susquehanna/Shale Hills Critical Zone Observatory. *Earth and Planetary Science Letters* **297**(1–2): 211–225.

Marechal JC, Dewandel B, Subrahmanyam K, Torri R. 2003. Specific methods for the evaluation of hydraulic properties in fractured hard-rock aquifers. *Current Science* **85**: 511–516.

Marechal JC, Dewandel B, Subrahmanyam K. 2004. Use of hydraulic tests at different scales to characterize fracture network properties in the weathered-fractured layer of a hard rock aquifer. *Water Resources Research* **40**: W11508. DOI: 10.1029/2004wr003137

Mavko G, Mukerji T. 1998. Bounds on low-frequency seismic velocities in partially saturated rocks. *Geophysics* **63**: 918.

McClymont AF, Roy JW, Hayashi M, Bentley LR, Maurer H, Langston G. 2011. Investigating groundwater flow paths within proglacial moraine using multiple geophysical methods. *Journal of Hydrology* **399**(1–2): 57–69.

Mindlin RD. 1949. Compliance of elastic bodies in contact. *Journal of Applied Mechanics – Transactions of the ASME* **16**: 259–268.

Molnar P, Anderson RS, Anderson SP. 2007. Tectonics, fracturing of rock, and erosion. *Journal of Geophysical Research – Earth Surfaces* **112**: F03014. DOI: 10.1029/2005jf000433

Moser TJ. 1991. Shortest path calculation of seismic rays. *Geophysics* **56**: 59–67.

National Research Council. 2001. *Basic Research Opportunities in Earth Science*. National Academy Press: Washington, DC.

Nur A, Mavko G, Dvorkin J, Galmudi D. 1998. Critical porosity: a key to relating physical properties to porosity in rocks. *The Leading Edge* **17**: 357–362.

Oldenburg DW, Li YG. 1999. Estimating depth of investigation in dc resistivity and IP surveys. *Geophysics* **64**: 403–416. DOI: 10.1190/1.1444545

Olhoeft GR. 1981. Electrical properties of granite with implications for the lower crust. *Journal of Geophysical Research - Solid Earth* **86**: 931–936. DOI: 10.1029/JB086iB02p00931

Olona J, Pulgar JA, Fernandez-Viejo G, Lopez-Fernandez C, Gonzalez-Cortina JM. 2010. Weathering variations in a granitic massif and related geotechnical properties through seismic and electrical resistivity methods. *Near Surface Geophysics* **8**: 585–599. DOI: 10.3997/1873-0604.2010043

Oster JL, Montanez IP, Sharp WD, Cooper KM. 2009. Late Pleistocene California droughts during deglaciation and Arctic warming. *Earth and Planetary Science Letters* **288**(3–4): 434–443.

Rasmussen C, Brantley S, Richter DD, Blum A, Dixon J, White AF. 2011. Strong climate and tectonic control on plagioclase weathering in granitic terrain. *Earth and Planetary Science Letters* **301**(3–4): 521–530.

Rawlinson N, Pozgay S, Fishwick S. 2010. Seismic tomography: a window into deep Earth. *Physics of the Earth and Planetary Interiors* **178**: 101–135. DOI: 10.1016/j.pepi.2009.10.002

Riebe CS, Granger DE. 2013. Quantifying effects of deep and near-surface chemical erosion on cosmogenic nuclides in soils, saprolite, and sediment. *Earth Surface Processes and Landforms* **38**(5): 523–533.

Riebe CS, Kirchner JW, Granger DE, Finkel RC. 2000. Erosional equilibrium and disequilibrium in the Sierra Nevada, inferred from cosmogenic Al-26 and Be-10 in alluvial sediment. *Geology* **28**(9): 803–806.

Riebe CS, Kirchner JW, Finkel RC. 2003. Long-term rates of chemical weathering and physical erosion from cosmogenic nuclides and geochemical mass balance. *Geochimica et Cosmochimica Acta* **67**(22): 4411–4427.

Riebe CS, Kirchner JW, Finkel RC. 2004. Erosional and climatic effects on long-term chemical weathering rates in granitic landscapes spanning diverse climate regimes. *Earth and Planetary Science Letters* **224**(3–4): 547–562.

Robinson DA, Binley A, Crook N, Day-Lewis FD, Ferré TPA, Grauch VJS, Knight R, Knoll M, Lakshmi V, Miller R, Nyquist J, Pellerin L, Singha K, Slater L. 2008. Advancing process-based watershed hydrological research using near-surface geophysics: a vision for, and review of, electrical and magnetic geophysical methods. *Hydrological Processes* **22**: 3604–3635. DOI: 10.1002/hyp.6963

Ruxton BP, Berry L. 1957. Weathering of granite and associated erosional features in Hong Kong. *Geological Society of America Bulletin* **68**(10): 1263.

Saarenketo T. 1998. Electrical properties of water in clay and silty soils. *Journal of Applied Geophysics* **40**: 73–88.

Samouëlian A, Cousin I, Tabbagh A, Bruand A, Richard G. 2005. Electrical resistivity survey in soil science: a review. *Soil and Tillage Research* **83**: 173–366. DOI: 10.1016/j.still.2004.10.004

Slater L, Binley A. 2006. Engineered barriers for pollutant containment and remediation. In *Applied Hydrogeophysics, NATO Science Series IV, Earth and Environmental Sciences*, Vereeken H, Binley A, Cassiani G, Revil A, Titov K (eds). Springer: Berlin; 293–317.

Stallard RF. 1985. River chemistry, geology, geomorphology, and soils in the Amazon and Orinoco Basins. In *The Chemistry of Weathering*, Drever JI (ed.). D. Reidel Publishing Company: Dordrecht; 293–316.

Stallard RF, Edmond JM. 1983. Geochemistry of the Amazon 2: the influence of geology and weathering environment on the dissolved-load. *Journal of Geophysical Research - Oceans and Atmospheres* **88**: 9671–9688.

Stock GM, Anderson RS, Finkel RC. 2004. Pace of landscape evolution in the Sierra Nevada, California, revealed by cosmogenic dating of cave sediments. *Geology* **32**(3): 193–196.

Stonestrom DA, White AF, Akstin KC. 1998. Determining rates of chemical weathering in soils – solute transport versus profile evolution. *Journal of Hydrology* **209**: 331–345.

Taylor R, Howard K. 2000. A tectono-geomorphic model of the hydrogeology of deeply weathered crystalline rock: evidence from Uganda. *Hydrogeology Journal* **8**: 279–573.

Wahrhaftig C. 1965. Stepped topography of southern Sierra Nevada California. *Geological Society of America Bulletin* **76**: 1165–1190. DOI: 10.1130/0016-7606

White AF, Blum AE, Schulz MS, Vivit DV, Stonestrom DA, Larsen M, Murphy SF, Eberl D. 1998. Chemical weathering in a tropical watershed, Luquillo mountains, Puerto Rico: I. Long-term versus short-term weathering fluxes. *Geochimica et Cosmochimica Acta* **62**(2): 209–226.

Winter TC. 1999. Relation of streams, lakes, and wetlands to groundwater flow systems. *Hydrogeology Journal* **7**: 28–45. DOI: 10.1007/s100400050178

Yoo K, Mudd SM, Sanderman J, Amundson R, Blum A. 2009. Spatial patterns and controls of soil chemical weathering rates along a transient hillslope. *Earth and Planetary Science Letters* **288**: 184–377.